How to cite: *Angew. Chem. Int. Ed.* **2023,** *62,* e202213806
International Edition: doi.org/10.1002/anie.202213806
German Edition: doi.org/10.1002/ange.202213806

Li-ion Batteries

Stabilizing Cobalt-free Li-rich Layered Oxide Cathodes through Oxygen Lattice Regulation by Two-phase Ru Doping

Yameng Fan, Emilia Olsson, Gemeng Liang, Zhijie Wang, Anita M. D'Angelo, Bernt Johannessen, Lars Thomsen, Bruce Cowie, Jingxi Li, Fangli Zhang, Yunlong Zhao, Wei Kong Pang, Qiong Cai,* and Zaiping Guo**

Abstract: The application of Li-rich layered oxides is hindered by their dramatic capacity and voltage decay on cycling. This work comprehensively studies the mechanistic behaviour of cobalt-free $Li_{1.2}Ni_{0.2}Mn_{0.6}O_2$ and demonstrates the positive impact of two-phase Ru doping. A mechanistic transition from the monoclinic to the hexagonal behaviour is found for the structural evolution of $Li_{1.2}Ni_{0.2}Mn_{0.6}O_2$, and the improvement mechanism of Ru doping is understood using the combination of in operando and post-mortem synchrotron analyses. The two-phase Ru doping improves the structural reversibility in the first cycle and restrains structural degradation during cycling by stabilizing oxygen (O^{2-}) redox and reducing Mn reduction, thus enabling high structural stability, an extraordinarily stable voltage (decay rate <0.45 mV per cycle), and a high capacity-retention rate during long-term cycling. The understanding of the structure-function relationship of $Li_{1.2}Ni_{0.2}Mn_{0.6}O_2$ sheds light on the selective doping strategy and rational materials design for better-performance Li-rich layered oxides.

Introduction

With the increasing demand for long-range electric vehicles, improving the energy density of rechargeable lithium-ion batteries (LIBs) is essential.[1] The limited theoretical capacity of traditional cathode materials solely based on transition metal (TM) redox has been a primary factor for the ceiling placed on the energy density of LIBs.[2] In this regard, Li-rich layered oxides (LLOs) have received a great deal of attention, due to their high reversible capacity ($>250\,mAh\,g^{-1}$) and high energy density ($900\,Wh\,kg^{-1}$), contributed by the TM redox and the additional O^{2-} redox. Unfortunately, LLOs suffer from dramatic voltage and capacity decay during cycling.[3] Substantial studies have been devoted to unravelling the origin of the decay.[4] It is well accepted that the direct causes of the voltage decay are the activation of low-voltage Mn^{2+}/Mn^{3+} and Co^{2+}/Co^{3+} redox couples and progressive structural rearrangements involving irreversible oxygen loss and TM migration.[5]

Based on established knowledge, a variety of strategies, such as surface modification,[3] cation doping,[6] and composition tuning,[7] have been employed to suppress voltage decay and capacity fading. Due to the lack of TM-O covalency, oxygen oxidation in 3*d*-TM-based LLOs ultimately ends with oxygen release, triggering TM migration and subsequent voltage decay.[8] Tarascon et al. investigated Li-rich $Li_2Ru_{1-y}M_yO_3$ (M = Ti, Sn) compounds and suggested that large or heavy cations, such as 4*d* metals, could be used to obviate the voltage decay issue by limiting the migration of TM ions and trapping these ions in tetrahedral

[*] Y. Fan, F. Zhang, Dr. W. K. Pang, Prof. Z. Guo
Faculty of Engineering, Institute for Superconducting & Electronic Materials, University of Wollongong
Wollongong, NSW 2500 (Australia)
E-mail: wkpang@uow.edu.au
q.cai@surrey.ac.uk
zaiping.guo@adelaide.edu.au

Y. Fan, Dr. Q. Cai
Department of Chemical and Process Engineering, University of Surrey
Guildford GU2 7XH (UK)
E-mail: q.cai@surrey.ac.uk

Dr. E. Olsson
Advanced Research Center for Nanolithography
Amsterdam 1098 XG (The Netherlands)
and
Institute for Theoretical Physics, University of Amsterdam
Amsterdam 1098 XH (The Netherlands)

Dr. G. Liang, Dr. Z. Wang, J. Li, F. Zhang, Prof. Z. Guo
School of Chemical Engineering & Advanced Materials, The University of Adelaide
Adelaide, SA 5005 (Australia)

Dr. A. M. D'Angelo, Dr. B. Johannessen, Dr. L. Thomsen, Dr. B. Cowie
Australian Synchrotron, Australian Nuclear Science and Technology Organization
Clayton, Victoria 3168 (Australia)

Dr. Y. Zhao
Advanced Technology Institute, University of Surrey
Guildford GU2 7XH (UK)

sites.[4a] Later, a series of studies on 4*d*- and 5*d*-TM-based LLOs confirmed that such heavy cations can mitigate voltage decay effectively by facilitating a reversible oxidation process rooted in their strong covalent bonding of TM(*d*)–O(*p*).[8,9] Nonetheless, the heavy metals-based LLOs are too penalizing for a practical application because of the relatively high cost and low energy density.

Doping 3*d*-TM-based LLOs with heavier cations might be a more feasible approach to improving performance.[10] Most recently, it was reported that a Zr-doped $Li_{1.21}Ni_{0.28}Mn_{0.51}O_2$ cathode, in which Li_2ZrO_3 slabs were constructed into Li_2MnO_3 domains,[10b] exhibits a low voltage decay rate (0.45 mV per cycle) due to the restrained formation of O_2 gas and TM reduction and migration. However, introducing inactive ions or components into LLOs is generally at the sacrifice of capacity. For example, the capacity delivered by the Zr-doped cathode is only $\approx$180 mAh g^{-1} at 1 C.

In addition, developing Co-free electrodes is inevitably the ultimate goal, considering that cobalt comes with a high cost and toxic issues unavoidably causing economic, ethical, and political issues.[11] Co-free LLO was first introduced by Thackeray's group,[12] where the Co-free Li-rich Mn-based $Li_{1.2}Ni_{0.2}Mn_{0.6}O_2$ (LNMO) cathode has been extensively studied.[13] However, the electrochemical performance of such LNMOs is significantly less satisfactory than the Co-based counterparts.[13c]

In this work, a small quantity (3 %) of the electrochemically active 4*d* metal, Ruthenium (Ru), is successfully doped into TM octahedral sites in both hexagonal and monoclinic phases in the typical Co-free Li-rich LNMO cathode. The effects of Ru doping on the structure and redox activities of the LNMO are investigated using various morphological, local structure, and crystallographic techniques. Neutron-based pair distribution function (PDF) analysis, neutron powder diffraction (NPD), and in operando synchrotron-based X-ray powder diffraction (XRPD) is employed to characterize the short- and long-range cation arrangement, the chemical environment of lattice oxygen, and the structural evolution on cycling. Post-mortem synchrotron-based near-edge X-ray absorption fine structure (NEXAFS) and X-ray absorption characterizations (XAS) are utilized to investigate the cationic/anionic redox process. The correlation between voltage decay with structural changes is reported in detail. Owing to enhanced structural stability, Ru-doped LNMO exhibits an extraordinarily low voltage decay (<0.45 mV per cycle) and meanwhile retains a high reversible capacity (215 mAh g^{-1} at 1 C) contributed by both cationic and O^{2-} redox. This work unravels the role of heavier ions in modifying the structural evolution and suppressing the voltage decay and sheds light on improving the performance of cathodes for practical applications in LIBs.

Results and Discussion

As-prepared Ru-doped $Li_{1.2}Ni_{0.2}Mn_{0.57}Ru_{0.03}O_2$ (LNMO-0.03Ru) and pristine LNMO show similar particle size and shape (Figure 1a and S1a, respectively). The transmission electron microscopy (TEM) image and corresponding energy dispersive spectroscopy (EDS) mapping demonstrate a homogeneous elemental distribution of Mn, Ni, Ru, and O (Figure 1b and 1c). Aberration-corrected scanning TEM (STEM) images in a high-angle annular dark-field (HAADF) mode depict the typical atomic arrangement of TM-Li sequences of monoclinic and hexagonal phases in the pristine and doped samples. The double-dot feature (TM-

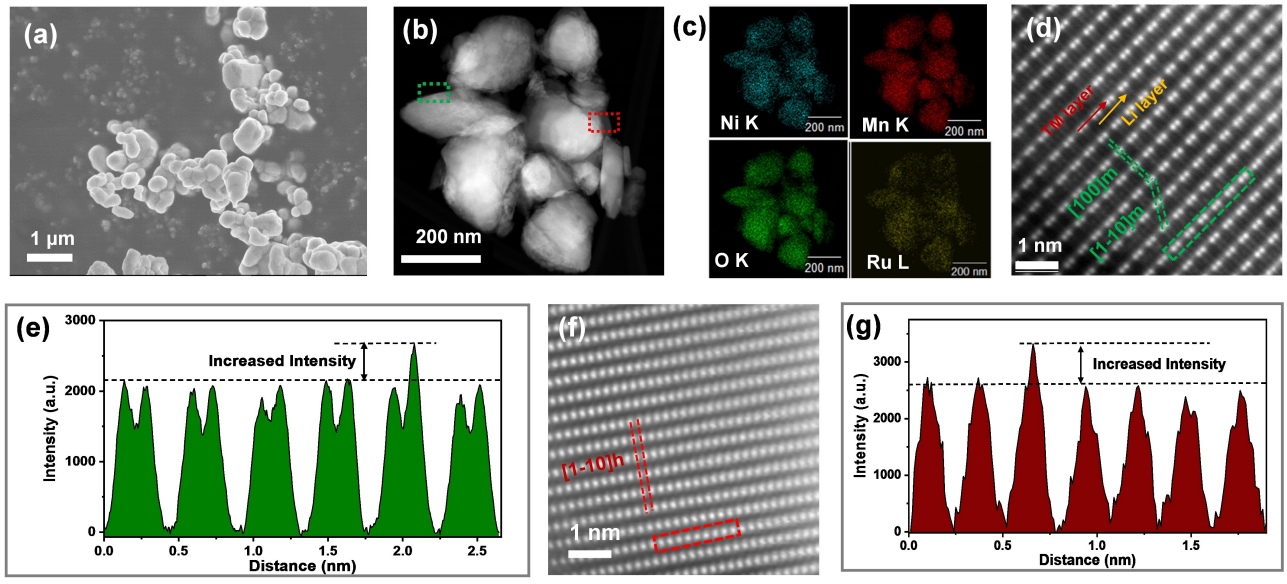

Figure 1. (a) SEM and (b) TEM images of the LNMO-0.03Ru sample; (c) Elemental distribution of Mn, Ni, Ru, and O in the LNMO-0.03Ru sample; (d, f) The HAADF-STEM images corresponding to the regions in (b) highlighted with a green box and red box, respectively; (e, g) Line profile analysis within the green box in (d) and the red in (f), respectively.

TM-Li-TM-TM) of the monoclinic phase in both materials can be seen in Figure 1d and S1c, respectively, which is consistent with previous reports.[14] Similarly, the single-dot (TM-TM) of the hexagonal phase is captured in both samples (Figure 1f and S1d).

Line profile analyses confirm that the larger-atomic-number Ru ions locate at the TM sites of both hexagonal and monoclinic phases, with the increased intensity along the double-dots (Figure 1e) and the single-dot (Figure 1g) features. Notably, the octahedral Ru has expanded the TM-TM distance by ≈3.3 % in the monoclinic phase (Figure S1e and 1e) and by ≈4.0 % in the hexagonal phase (Figure S1f and 1g). This result reveals that the Ru introduction affected both phases of the LNMOs. The close formation energies of Ru in the hexagonal and monoclinic phase further confirmed the two-phase doping (Figure S12).

X-ray photoelectron spectroscopy (XPS) is used to investigate the Ru doping state. The Ru 3*d* core spectra changed significantly in LNMO-0.03Ru (Figure 2a). Compared with RuO_2, the Ru $3d_{5/2}$ binding energy for the LNMO-0.03Ru shifts to ≈282 eV, confirming that Ru^{4+} is octahedrally bonded in layered oxides.[4a,9b] Rietveld refinement was performed against XRPD and NPD data (Figure 2b, 2c, and S2). The XRPD and NPD patterns are fitted well based on a two-phase model containing a hexagonal ($R\bar{3}m$ space group) phase[15] and a monoclinic (*C2/c* space group) phase.[16] This agrees with the fitting result of their neutron-based PDF data using the two structural models (Figure S3). The refined results (Table S1 and Table S2) suggest that the lattice expansion of both *C2/c* and $R\bar{3}m$ phases upon Ru doping, showing excellent agreement with the STEM analyses and demonstrating a solid proof of Ru distribution in two domains. The similar XRPD and NPD profiles and their intergrown feature have further complicated the refinement process. Determining Ru site occupancy (%) is beyond the data limitation. Furthermore, upon Ru doping, the weight fraction of the *C2/c* phase decrease from 60(2) to 48(1) wt %,[17] which might be related to the increased complication of cation mixing and the intergrown feature.

Interestingly, the two phases are marginally different in crystallography (Table S1 and S2). The minor dissimilarities can be observed by comparing the TM-O bond lengths and establishing the Bond-Valence-Sum (BVS) calculation. Notably, all TM sites in *C2/c* and $R\bar{3}m$ phases are shared by Mn and Ni (or Li), resulting in the underestimation of the Mn valence. However, the calculated BVS values are informative. The higher BVS implies the Mn valence is closer to +4, while the lower BVS indicates a higher mixing degree with Li/Ni. For the *C2/c* phase with Li/Mn mixing only, the order of Li concentration at Mn sites is Mn1 > Mn3 > Mn2 in both samples, despite the Ru inclusion. For $R\bar{3}m$ phase, the lower BVS in LNMO-0.03Ru may suggest higher Li/Ni mixing, which is supported by the intensity ratio of peak (003)/(104) in XRPD, indicative of the Li/Ni mixing in the $R\bar{3}m$ phase.[18] Li/Ni mixing is reported to improve voltage retention by precluding the formation of O–O dimers.[19]

The initial charge/discharge curves (Figure 3a) show that LNMO-0.03Ru has a lower oxygen activation plateau than LNMO, indicating the enhanced Li diffusion in LNMO-0.03Ru, due to the enlarged diffusion channels and lattice volume. The higher Li^+ diffusion coefficient of LNMO-0.03Ru is confirmed by the galvanostatic intermittent titration technique (GITT, Figure S4). LNMO-0.03Ru delivers a similar initial charge capacity as LNMO but a higher discharge capacity (≈280 mAh g^{-1}), leading to a higher initial Coulombic efficiency (ICE, ≈83 %). The electrochemical performance of LNMO with different Ru doping contents (Figure S5) demonstrates that Ru can improve the electrochemical performance of LNMO effectively. However, the capacity drops at 5 % Ru doping, which may be due to poor crystallisation (Figure S6). In this regard, 3 % Ru is the focus of this work. Notably, LNMO-0.03Ru exhibits a better rate capability (≈162 mAh g^{-1} at 5 C, Figure 3b) and a significantly enhanced capacity retention, especially for long cycling, at 1 C (Figure 3c). After 500 cycles, the capacity retention rate for LNMO is only 31 %, while that for LNMO-0.03Ru remains up to 74 %.

Meanwhile, a noticeable voltage decay occurs in LNMO (Figure 3d), but the discharge curves for LNMO-0.03Ru remain almost unchanged along the cycling (Figure 3e). This was further investigated using dQ/dV curves (Figure 3f). The dQ/dV discharge peaks almost resemble in LNMO-0.03Ru, while the ones of LNMO show a distinct downshift to the low potential region upon cycling, suggesting the occurrence of voltage decay. A new peak around 2.9 V occurs for the LNMO after 200 cycles, indicating significant

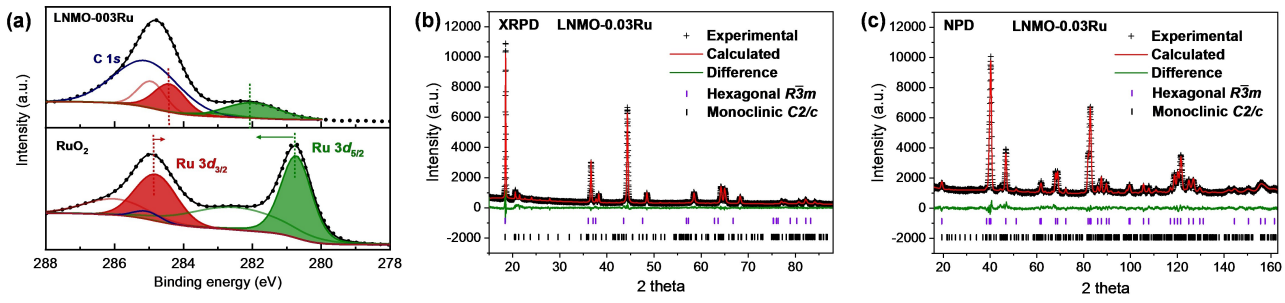

Figure 2. (a) Ru 3*d* XPS spectra of RuO_2 and LNMO-0.03Ru; joint Rietveld refinement profiles using (b) XRPD and (c) NPD data of LNMO-0.03Ru (R_{wp} = 5.789 %, combined GOF = 1.56, the $R\bar{3}m$ phase = 52(1) wt %, the *C2/c* phase = 48(1) wt %).

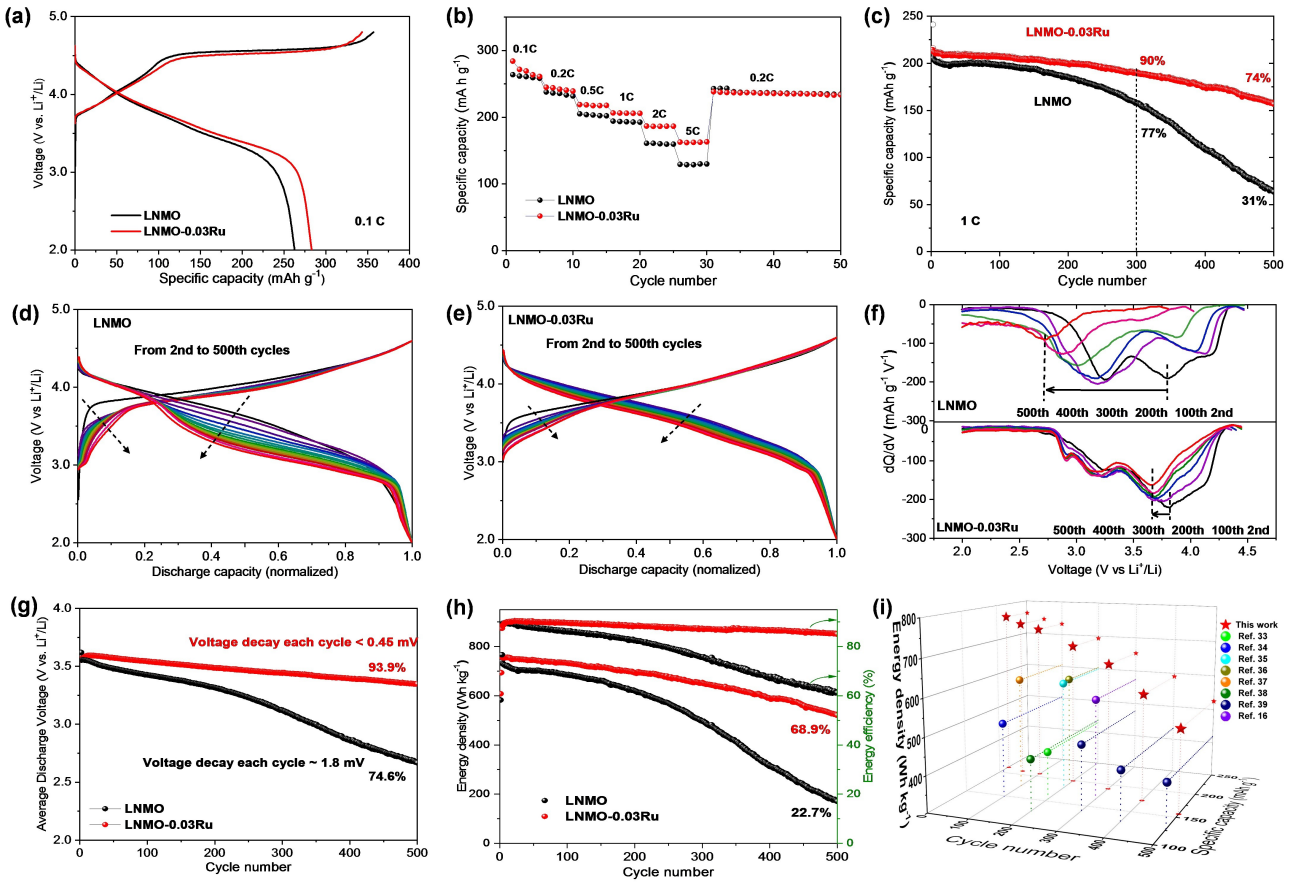

Figure 3. (a) The 1st charge/discharge curves, (b) rate capability, and (c) cycling performance of LNMO and LNMO-0.03Ru; normalised charge/discharge curves of (d) LNMO and (e) LNMO-0.03Ru, respectively, collected every 25 cycles; (f) Comparison of voltage decay in dQ/dV curves of LNMO and LNMO-0.03Ru, where the arrows highlight the shift of the profile; (g) Average discharge voltage and (h) energy density of LNMO and LNMO-0.03Ru at 1 C. At least five coin cells were averaged for each data set. The error for the specific capacity is approximately ± 3 mAh g^{-1}. (i) Energy and capacity performance comparison of LNMO-0.03Ru with other Co-free LLOs previously reported.

charge compensation from $Mn^{3+/4+}$.[20] The presence of unstable Mn^{3+} inevitably leads to the formation of undesirable Mn^{2+} and, thus, Mn dissolution into electrolytes.[1] A similar tendency was verified using cyclic voltammetry (CV) curves (Figure S7). No additional peaks for Ru redox were observed, possibly due to the small doping amount of Ru.

In all, the average voltage decay for LNMO in 500 cycles is $\approx$1.8 mV per cycle; in contrast, LNMO-0.03Ru exhibits negligible voltage decay ($<$0.45 mV per cycle) (Figure 3g), which is significantly reduced compared with other previously reported LLOs (Table S3). The energy retention rate of LNMO-0.03Ru is improved by $>$300 %, compared with that of LNMO (Figure 3h). To our knowledge, the energy performance of LNMO-0.03Ru is remarkably high, superior to other reported Co-free LLOs (Figure 3i).[10b,21] It is unambiguous that Ru doping can lead to a high energy density by improving the capacity and suppressing voltage decay and formation of undesirable Mn^{2+} and thus Mn dissolution into electrolytes.

The structure evolution was investigated using in operando synchrotron-based XRPD. LNMO and LNMO-0.03Ru are similar in the 1st and 50th cycles (Figure 4). The reflections at 8.3 and 19.5° represent the *d*-spacing of $\approx$4.76 and $\approx$2.03 Å, which are usually regarded as 003 and 104 of the $R\bar{3}m$ phase.[17b] The *c* variation can then be explained to be originated from the electrostatic repulsion of TMO_6 layers[22] and the increased attractive van der Waals interactions,[23] respectively, upon different degrees of lithiation. The continuous decrease of *a* is due to the oxidation and decreasing ionic radii of the TM ($Ni^{2+}/Ni^{3+}/Ni^{4+}$ and Mn^{3+}/Mn^{4+}) ions. Typically, $LiNi_xCo_yMn_zO_2$ (NCM, $R\bar{3}m$) undergoes various phase transformations during charging, from hexagonal H1, via a monoclinic M and a hexagonal H2, to the hexagonal H3 phases.[24] Thus, these reflections undergo a non-NCM-type evolution in the first cycle (Figure 4a and 4c). After 50 cycles, different mechanistic behaviour is observed (Figure 4b and 4d). *c* increases on the initial charging and sharply decreases upon further charging to 4.8 V. A reversed evolution of the *c* value is observed when the Li is inserted into the structure. It is undoubtedly a typical $R\bar{3}m$ behaviour, which has been widely observed in NCM.[25] Unlike the typical NCM, O^{2-} redox occurs at $>$4.3 V in LLOs, resulting in the reduced attractive force between TM and O and the stable *a* value. Even though

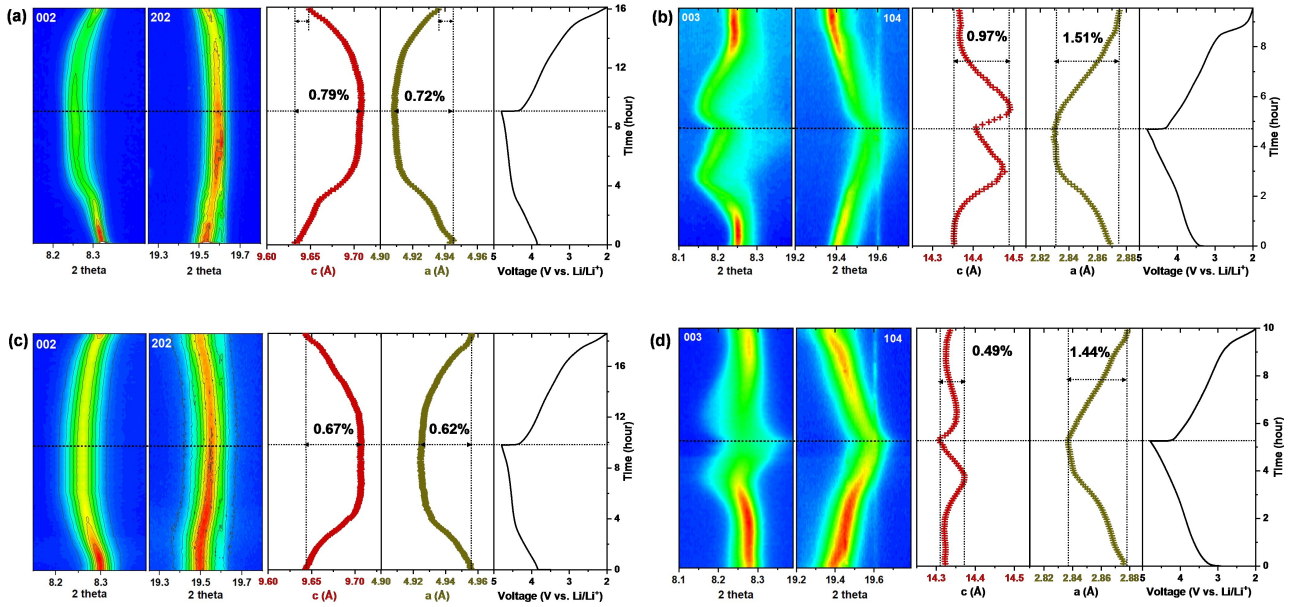

Figure 4. Contour plot of in operando synchrotron XRPD data and corresponding single peak fitting results and electrochemical voltage curves of cells containing the undoped LNMO (a) at the first cycle at 0.1 C and (b) after 50 cycles at 0.2 C and LNMO-0.03Ru (c) at the first cycle at 0.1 C and (d) after 50 cycles at 0.2 C. Note that the *C*2/*c* structural model was used for the fitting of the electrodes at the first cycle, while the $R\bar{3}m$ structural model was for after 50 cycles.

XRPD of *C*2/*c* and $R\bar{3}m$ are nearly indistinguishable, their lattice responses upon lithium insertion and desertion tell the difference.

Previous studies mostly regard LLO as a $R\bar{3}m$ phase for convenience and ignore the presence of the *C*2/*c* phase.[26] As confirmed in diffraction and PDF analyses (Figure 2b, 2c, and S3), the *C*2/*c* component or domain has a significant weight, resulting that LLOs being different from the typical NCM in terms of phase evolution. The structural changes observed in both samples during the first cycle are likely *C*2/*c* behaviour. Thus, a mechanistic behaviour transition from *C*2/*c* to $R\bar{3}m$ occurs after cycling.

In comparison, LNMO-0.03Ru shows lower lattice changes in *c* (0.67 %) and *a* (0.62 %) compared with the variation of *c* (0.79 %) and *a* (0.72 %) in LNMO during the first charge. The improved structural stability of ≈15.2 % and ≈8.9 %, along with the *c* and *a* axes, respectively, demonstrate the origins of better capacity and energy retention, directly showing the positive impact of Ru doping on the LLO. Moreover, the *c* and *a* values are fully reversible, indicating a highly reversible structural change in LNMO-0.03Ru. Notably, the improvement in the structural stability of LNMO-0.03Ru is intensified, compared with LNMO, after cycling. LNMO-0.03Ru exhibits a remarkably restrained structural change at the high potential region, especially along the *c* axis, where 0.49 % is for LNMO-0.03Ru, and 0.97 % is for LNMO. The strain evolution (Figure S13) during charge-discharge further demonstrated that Ru doping effectively improves the structure stability of LNMO-0.03Ru against lithiation and delithiation processes.

O K edge spectra are compared as a function of the state-of-charge (SOC) (Figure 5a). The pre-edge region (525–534 eV) reflects the hybridization of O 2*p* and TM 3*d* orbitals (Figure 5b and 5e), where peak A and peak C correspond to t_{2g} (plus e_g spin-up) and e_g (spin-down) states, respectively.[4b] Due to the full t_{2g} and half-full e_g orbitals of Ni^{2+} (t_{2g}^6 e_g^2), the hybridization of O 2*p* and Ni 3*d* orbitals is only related to peak C, while peak A is mainly assigned to the hybridization of O 2*p* and Mn 3*d* orbitals (Mn^{3+}: t_{2g}^4 e_g^0, Mn^{4+}: t_{2g}^3 e_g^0). The new peak (labelled as peak B in Figure 5b and 5e), which gradually appears during the charging process, is used to characterise the O^{2-} redox reaction.[10b,27] Peak B appears in LNMO-0.03Ru (Figure 5e) when charged to 4.3 V, while it does not appear in LNMO until 4.5 V (Figure 5b), suggesting a lower activation polarisation of O^{2-} redox after Ru doping. Peak B reaches the maximum intensity at 4.8 V in both LNMO and LNMO-0.03Ru. Upon discharge, peak B disappears in LNMO-0.03Ru at 3.6 V, but does not disappear entirely in LNMO even at 2.0 V, indicating the high O^{2-} redox reversibility in LNMO-0.03Ru and agreeing with the dQ/dV results (Figure 3f). Considerably, the Ru inclusion has modified the O-metal chemical environment and minimized the voltage decay. The integrated intensity of the pre-edge peaks (525–534 eV, Figure 5d), relative to that of the open-circuit voltage (OCV), can be used to reflect the density of hole states (DOHS) in the O 2*p* and TM 3*d* orbitals.[13a,28] DOHS are similar at high charge for two samples, while LNMO-0.03Ru is relatively closer to its initial state at high discharge, manifesting higher reversibility. Furthermore, the DOHS for LNMO-0.03Ru shows a sudden drop associated with the disappearance of peak B, verifying that O^{2-} redox largely accounts for the discharge capacity at the high potential region. Such findings

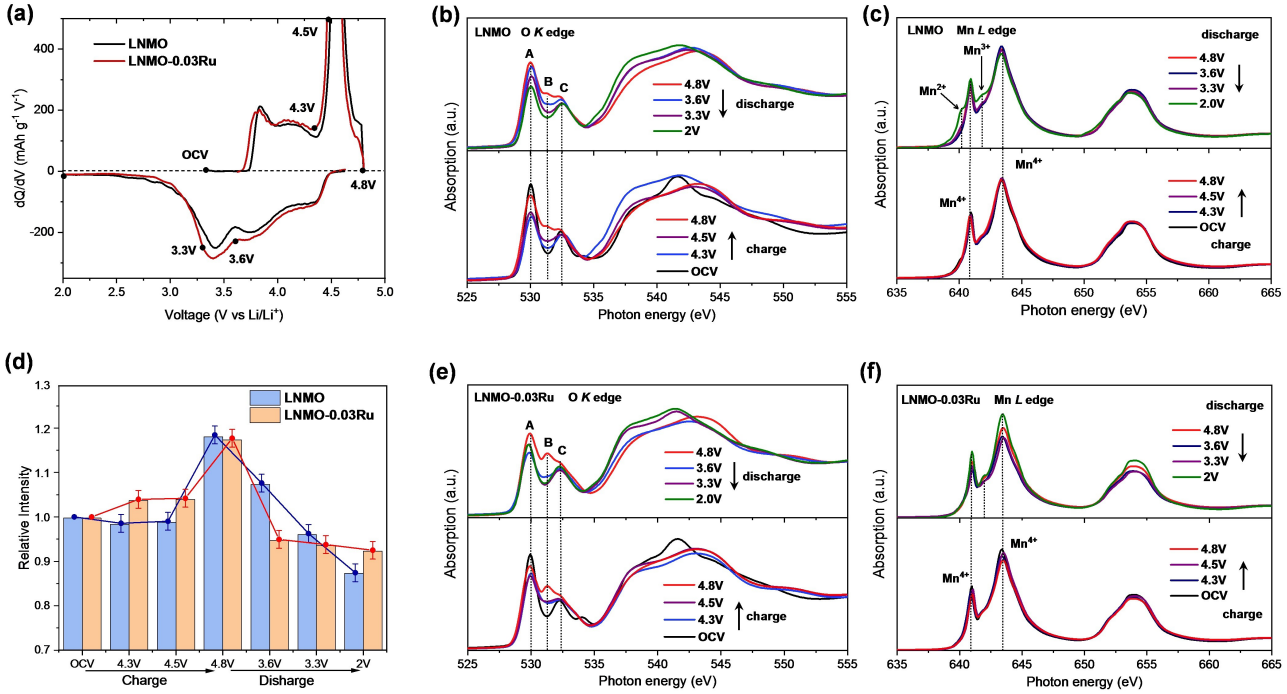

Figure 5. (a) *dQ/dV* curves with the corresponding SOCs marked; (b) O K edge and (c) Mn L edge spectra of post-mortem samples of LNMO; (e) O K edge and (f) Mn L edge spectra of post-mortem samples of LNMO-0.03Ru; (d) Relative integrated intensity variation of the pre-edge peaks (525–534 eV).

are further supported by post-mortem XPS analyses (Figure S8).

Mn valences can be identified through the peak positions (photon energies) of Mn L-edge spectra (Figure 5c and 5f). Mn^{4+} owns a major peak (643.5 eV) and a shoulder peak (640.9 eV), whilst Mn^{3+} has a peak at 641.8 eV, and Mn^{2+} has a signal at 640.2 eV.[10b] For both materials, typical Mn^{4+} signals remain unchanged during the first charging process. On discharge, the signals of Mn^{2+} and Mn^{3+} can be distinctly observed in LNMO, but barely seen in LNMO-0.03Ru, except for a tiny amount of Mn^{3+} formed at 2.0 V. This is verified by the Mn K edge results (Figure S9a and S9b). The restrained formation of Mn^{2+} and Mn^{3+} fully supports our finding of enhanced structural stability as ascertained via in operando XRPD. After 50 cycles, LNMO-0.03Ru still has a relatively lower Mn reduction than in LNMO (Figure S10). In addition, Ni and Ru contribute to capacity as fully-reversible cationic redox centres in LNMO-0.03Ru, as revealed by the variation of Ni K edge (Figure S9c) and the combination of Ru K-edge (FigureS9d) and Ru 3*p* XPS spectra (Figure S8c), consistent with previous studies.[29]

To further examine the effects of Ru doping on the oxygen lattice, the oxygen vacancy formation energy ($E_f(V_O)$) in both $R\bar{3}m$ (h-LNMO) and $C2/c$ (m-LNMO) phases were calculated for each oxygen site in the lattices (24 sites per system). A higher $E_f(V_O)$ indicates that the defect concentration under equilibrium conditions is lower than for a lower $E_f(V_O)$. All $E_f(V_O)$ for the undoped and doped (Ru_{TM}) systems are presented in Figure 6. This is similar to the site dependence observed for $Ru_{TM,}$ which also

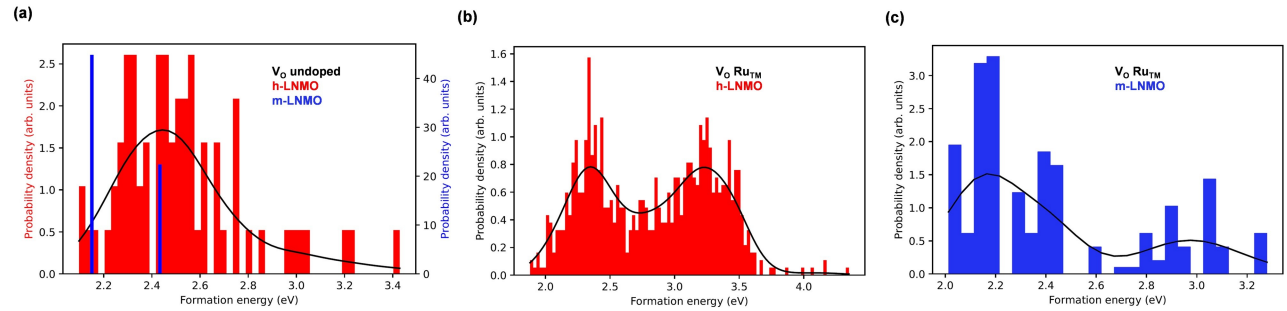

Figure 6. Calculated $E_f(V_O)$ for (a) undoped LNMO, (b) h-LNMO with Ru substituted on TM sites, and (c) m-LNMO with Ru substituted on TM sites. The black trendlines are included as a guide for the eyes.

showed a clear environmental impact (Figure S11 and S12). In Figure 6b and 6c, it is clear that Ru-doping introduces distinct V_O environments that were not observed in the undoped systems (Figure 6a), indicating a degree of Ru dependence for the V_O. V_O sites directly next to the Ru_{TM} sites show higher $E_f(V_O)$ (second hump in Figure 6b) than those further away from the dopant site. Examining the average formation energies (Table S10), it is clear that there is a shift to higher energies in the average $E_f(V_O)$ upon Ru-doping from an average $E_f(V_O)=2.52$ eV to $E_f(V_O)=2.83$ eV for h-LNMO, and $E_f(V_O)=2.24$ eV to $E_f(V_O)=2.42$ eV for m-LNMO. Hence, it can be concluded that Ru-doping of the LNMO structure could stabilise the oxygen lattice locally, supporting the experimentally observed strengthening of the O lattice. Moreover, it has been shown that not only does the Ru-doping itself have an impact on the stability of the O lattice, but also the position of the Ru dopant.

Combining the in operando, post-mortem mechanistic, and computational studies, the mechanistic behaviour of LLOs and the role of Ru dopants in the structural evolution can be understood and are schematically summarized in Scheme 1. The LLO undergoes oxidation of TM and a subsequent charge deficiency of O^{2-}, resulting in a non-NCM mechanistic response on the first charge. Upon cycling, the layered structure of LLO is transitioning from the *C2/c* type to $R\bar{3}m$ type dominant. It should be noted that this *C2/c* to $R\bar{3}m$ transition is an intrinsic mechanistic behaviour of LLOs, as it is found for both the undoped LNMO and LNMO-0.03Ru. The observed structural evolution reveals that structural degradation is attributed to the enormous O lattice change upon the anion redox during cycling. At a high delithiated state, the existence of deficient O^{2-} (or O^{n-}) loosens the honeycomb and layered structure of LLO and may escape, as O_2, from the lattice.[17b,30] In this regard, Ru^{4+} present in both two phases can significantly restrain the lattice changes by stabilizing the lattice with the strong bonding of Ru^{4+}-O^{2-} and Ru^{5+} strengthen the O lattice during O^{2-} deficiency at the high potential region, facilitating the positive impact of the Ru doping on LLOs' structural stability and performance. Notably, the presence of Ru in both *C2/c* and $R\bar{3}m$ phase effectively improves the solidity of O lattice in the first cycle, enables superior structural stability against delithiation and lithiation, and inhibits the formation of low-valence Mn and the resulting dissolution, minimizing voltage and capacity decay along with cycling. The poor cycling performance of LNMO, or typical LLOs, can be unambiguously attributed to their intrinsic structural degradation. The involvement of strong covalent bonding of Ru-O has brought the LNMO an enhanced oxygen lattice stability and a significantly improved structure stability against lithiation and delithiation processes.

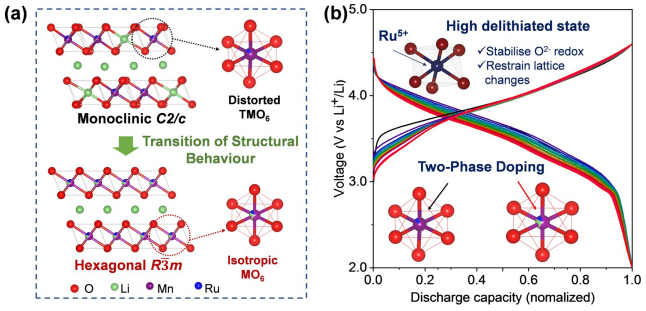

Scheme 1. Schematic illustration of the (a) structural evolution and (b) Ru doping effects on LNMO.

Conclusion

4*d*-metal Ru is successfully doped to octahedral sites of both *C2/c* and $R\bar{3}m$ domains of Li-rich Mn-based layered $Li_{1.2}Ni_{0.2}Mn_{0.6}O_2$ cathode material, which has been comprehensively evidenced in our work. The sample with 3 % Ru doping demonstrates a voltage retention rate of ≈93.9 % (4.5 mV per cycle) and energy retention of ≈69 % after 500 cycles at 1 C. The enhanced mechanism by Ru doping has been comprehensively studied, and it is confirmed that strong Ru-O bonding enhances the structure reversibility of the layered structure against delithiation and lithiation. Ru is electrochemically active, and the presence of Ru^{5+} strengthens the O lattice during O^{2-} redox, substantially inhibiting the dramatic structural changes and warrants structural stability in long-term cycling at a highly delithiated state. While Ru is introduced, the Mn reduction is effectively restrained within the LLO structure, further enhancing the structural stability. It should be noteworthy that the mechanistic transition from *C2/c* to $R\bar{3}m$ of LLOs along cycling is for the first time reported in this work. The findings here may inspire new ideas on designing and stabilizing the structure of other layered Li-rich oxides and other advanced cathode materials involving O^{2-} redox.

Acknowledgements

Part of this work was carried out at the Powder Diffraction beamline (beamtime: M17195), the wiggler XAS beamline (12-ID) (beamtime: M17591), the Soft X-ray (SXR) beamline (beamtime: M17449) at the Australian Synchrotron, and Echidna (beamtime: MI7601) at the Australian Centre for Neutron Scattering under merit programs. The authors acknowledge the operational support of ANSTO staff, especially Prof. Vanessa K. Peterson, for collecting NPD. The authors thank Dr. Jue Liu of Oak Ridge National Laboratory for the neutron-based PDF data collection. The authors acknowledge the Electron Microscopy Centre, University of Wollongong, for their support and equipment assistance. Y. F. is grateful for the joint Surrey-Wollongong PhD studentship. Computational work was carried out at the Advanced Research Center for Nanolithography, a public-private partnership of the University of Amsterdam, the Vrije Universiteit Amsterdam, the University of Groningen, the Dutch Research Council, and the semiconductor equipment manufacturer ASML. It used the Dutch national e-infrastructure with the support of the SURF Cooperative

using grant no. EINF-2434, and we thank SURF (http://www.surf.nl) for the support in using the Lisa Compute Cluster and National Supercomputer Snellius. E. O. is grateful for a WISE Fellowship from the Dutch Research Council. Open Access publishing facilitated by The University of Adelaide, as part of the Wiley - The University of Adelaide agreement via the Council of Australian University Librarians.

Conflict of Interest

The authors declare no conflict of interest.

Data Availability Statement

The data that support the findings of this study are available from the corresponding author upon reasonable request.

Keywords: Lattice Oxygen · Li-Rich Cathodes · Lithium-Ion Batteries · Structural Evolution · Voltage Decay

[1] G. Liang, V. K. Peterson, Z. Wu, S. Zhang, J. Hao, C. Z. Lu, C. H. Chuang, J. F. Lee, J. Liu, G. Leniec, S. M. Kaczmarek, A. M. D'Angelo, B. Johannessen, L. Thomsen, W. K. Pang, Z. Guo, *Adv. Mater.* **2021**, *33*, 2101413.

[2] a) S. Hu, A. S. Pillai, G. Liang, W. K. Pang, H. Wang, Q. Li, Z. Guo, *Electrochem. Energy Rev.* **2019**, *2*, 277–311; b) M. Han, J. Jiao, Z. Liu, X. Shen, Q. Zhang, H.-J. Lin, C.-T. Chen, Q. Kong, W. K. Pang, Z. Guo, R. Yu, L. Gu, Z. Hu, Z. Wang, L. Chen, *Adv. Energy Mater.* **2020**, *10*, 1903634.

[3] S. Hu, Y. Li, Y. Chen, J. Peng, T. Zhou, W. K. Pang, C. Didier, V. K. Peterson, H. Wang, Q. Li, Z. Guo, *Adv. Energy Mater.* **2019**, *9*, 1901795.

[4] a) M. Sathiya, A. M. Abakumov, D. Foix, G. Rousse, K. Ramesha, M. Saubanère, M. L. Doublet, H. Vezin, C. P. Laisa, A. S. Prakash, D. Gonbeau, G. VanTendeloo, J. M. Tarascon, *Nat. Mater.* **2015**, *14*, 230–238; b) S. Myeong, W. Cho, W. Jin, J. Hwang, M. Yoon, Y. Yoo, G. Nam, H. Jang, J.-G. Han, N.-S. Choi, M. G. Kim, J. Cho, *Nat. Commun.* **2018**, *9*, 3285.

[5] a) E. Hu, X. Yu, R. Lin, X. Bi, J. Lu, S. Bak, K.-W. Nam, H. L. Xin, C. Jaye, D. A. Fischer, K. Amine, X.-Q. Yang, *Nat. Energy* **2018**, *3*, 690–698; b) D. Eum, B. Kim, S. J. Kim, H. Park, J. Wu, S. P. Cho, G. Yoon, M. H. Lee, S. K. Jung, W. Yang, W. M. Seong, K. Ku, O. Tamwattana, S. K. Park, I. Hwang, K. Kang, *Nat. Mater.* **2020**, *19*, 419–427.

[6] Y. Fan, W. Zhang, Y. Zhao, Z. Guo, Q. Cai, *Energy Storage Mater.* **2021**, *40*, 51–71.

[7] K. Ku, J. Hong, H. Kim, H. Park, W. M. Seong, S.-K. Jung, G. Yoon, K.-Y. Park, H. Kim, K. Kang, *Adv. Energy Mater.* **2018**, *8*, 1800606.

[8] M. Saubanère, E. McCalla, J.-M. Tarascon, M.-L. Doublet, *Energy Environ. Sci.* **2016**, *9*, 984–991.

[9] a) E. McCalla, A. M. Abakumov, M. Saubanère, D. Foix, E. J. Berg, G. Rousse, M.-L. Doublet, D. Gonbeau, P. Novák, G. Van Tendeloo, *Science* **2015**, *350*, 1516–1521; b) M. Sathiya, G. Rousse, K. Ramesha, C. P. Laisa, H. Vezin, M. T. Sougrati, M. L. Doublet, D. Foix, D. Gonbeau, W. Walker, A. S. Prakash, M. Ben Hassine, L. Dupont, J. M. Tarascon, *Nat. Mater.* **2013**, *12*, 827–835; c) Y. Yu, P. Karayaylali, D. Sokaras, L. Giordano, R. Kou, C.-J. Sun, F. Maglia, R. Jung, F. S. Gittleson, Y. Shao-Horn, *Energy Environ. Sci.* **2021**, *14*, 2322–2334.

[10] a) M. Zubair, G. Li, B. Wang, L. Wang, H. Yu, *ACS Appl. Energy Mater.* **2019**, *2*, 503–512; b) J. Zhang, Q. Zhang, D. Wong, N. Zhang, G. Ren, L. Gu, C. Schulz, L. He, Y. Yu, X. Liu, *Nat. Commun.* **2021**, *12*, 3071.

[11] B. K. Sovacool, *Extr. Ind. Soc.* **2019**, *6*, 915–939.

[12] C. S. Johnson, J. S. Kim, C. Lefief, N. Li, J. T. Vaughey, M. M. Thackeray, *Electrochem. Commun.* **2004**, *6*, 1085–1091.

[13] a) K. Luo, M. R. Roberts, N. Guerrini, N. Tapia-Ruiz, R. Hao, F. Massel, D. M. Pickup, S. Ramos, Y. S. Liu, J. Guo, A. V. Chadwick, L. C. Duda, P. G. Bruce, *J. Am. Chem. Soc.* **2016**, *138*, 11211–11218; b) F. Wu, G. T. Kim, T. Diemant, M. Kuenzel, A. R. Schür, X. Gao, B. Qin, D. Alwast, Z. Jusys, R. J. Behm, *Adv. Energy Mater.* **2020**, *10*, 2001830; c) A. Celeste, M. Tuccillo, A. Santoni, P. Reale, S. Brutti, L. Silvestri, *ACS Appl. Energy Mater.* **2021**, *4*, 11290–11297.

[14] K. A. Jarvis, Z. Deng, L. F. Allard, A. Manthiram, P. J. Ferreira, *Chem. Mater.* **2011**, *23*, 3614–3621.

[15] D. Caurant, N. Baffler, V. Bianchi, G. Grégoire, S. Bach, *J. Mater. Chem.* **1996**, *6*, 1149–1155.

[16] D. Pasero, V. McLaren, S. de Souza, A. R. West, *Chem. Mater.* **2005**, *17*, 345–348.

[17] a) C. Yin, Z. Wei, M. Zhang, B. Qiu, Y. Zhou, Y. Xiao, D. Zhou, L. Yun, C. Li, Q. Gu, W. Wen, X. Li, X. Wen, Z. Shi, L. He, Y. Shirley Meng, Z. Liu, *Mater. Today* **2021**, *51*, 15–26; b) D. Mohanty, S. Kalnaus, R. A. Meisner, K. J. Rhodes, J. Li, E. A. Payzant, D. L. Wood, C. Daniel, *J. Power Sources* **2013**, *229*, 239–248.

[18] N. Li, M. Sun, W. H. Kan, Z. Zhuo, S. Hwang, S. E. Renfrew, M. Avdeev, A. Huq, B. D. McCloskey, D. Su, W. Yang, W. Tong, *Nat. Commun.* **2021**, *12*, 2348.

[19] a) J. Zhang, F. Cheng, S. Chou, J. Wang, L. Gu, H. Wang, H. Yoshikawa, Y. Lu, J. Chen, *Adv. Mater.* **2019**, *31*, 1901808; b) J. L. Shi, J. N. Zhang, M. He, X. D. Zhang, Y. X. Yin, H. Li, Y. G. Guo, L. Gu, L. J. Wan, *ACS Appl. Mater. Interfaces* **2016**, *8*, 20138–20146.

[20] G. Assat, D. Foix, C. Delacourt, A. Iadecola, R. Dedryvère, J.-M. Tarascon, *Nat. Commun.* **2017**, *8*, 2219.

[21] a) L. Bao, L. Wei, N. Fu, J. Dong, L. Chen, Y. Su, N. Li, Y. Lu, Y. Li, S. Chen, *J. Energy Chem.* **2022**, *66*, 123–132; b) E. Zhao, X. Liu, H. Zhao, X. Xiao, Z. Hu, *Chem. Commun.* **2015**, *51*, 9093–9096; c) C. Zhang, B. Wei, W. Jiang, M. Wang, W. Hu, C. Liang, T. Wang, L. Chen, R. Zhang, P. Wang, W. Wei, *ACS Appl. Mater. Interfaces* **2021**, *13*, 45619–45629; d) H. Liu, W. Xiang, C. Bai, L. Qiu, C. Wu, G. Wang, Y. Liu, Y. Song, Z.-G. Wu, X. Guo, *Ind. Eng. Chem. Res.* **2020**, *59*, 19312–19321; e) A. Abdel-Ghany, A. M. Hashem, A. Mauger, C. M. Julien, *Energies* **2020**, *13*, 3487; f) F. Wu, G. T. Kim, M. Kuenzel, H. Zhang, J. Asenbauer, D. Geiger, U. Kaiser, S. Passerini, *Adv. Energy Mater.* **2019**, *9*, 1902445; g) C. Han, J. Wu, S. Li, T. Li, J. Li, H. Liu, *Solid State Ionics* **2021**, *364*, 115629.

[22] M. Ma, N. A. Chernova, B. H. Toby, P. Y. Zavalij, M. S. Whittingham, *J. Power Sources* **2007**, *165*, 517–534.

[23] M. Aykol, S. Kim, C. Wolverton, *J. Phys. Chem. C* **2015**, *119*, 19053–19058.

[24] L. de Biasi, B. Schwarz, T. Brezesinski, P. Hartmann, J. Janek, H. Ehrenberg, *Adv. Mater.* **2019**, *31*, 1900985.

[25] A. O. Kondrakov, A. Schmidt, J. Xu, H. Geßwein, R. Mönig, P. Hartmann, H. Sommer, T. Brezesinski, J. Janek, *J. Phys. Chem. C* **2017**, *121*, 3286–3294.

[26] a) X. Li, Y. Qiao, S. Guo, Z. Xu, H. Zhu, X. Zhang, Y. Yuan, P. He, M. Ishida, H. Zhou, *Adv. Mater.* **2018**, *30*, 1705197; b) H. Zheng, C. Zhang, Y. Zhang, L. Lin, P. Liu, L. Wang, Q. Wei, J. Lin, B. Sa, Q. Xie, D. L. Peng, *Adv. Funct. Mater.* **2021**, *31*, 2100783.

[27] Q. Li, D. Zhou, L. Zhang, D. Ning, Z. Chen, Z. Xu, R. Gao, X. Liu, D. Xie, G. Schumacher, X. Liu, *Adv. Funct. Mater.* **2019**, *29*, 1806706.
[28] S. Hy, W.-N. Su, J.-M. Chen, B.-J. Hwang, *J. Phys. Chem. C* **2012**, *116*, 25242–25247.
[29] a) N. Li, S. Hwang, M. Sun, Y. Fu, V. S. Battaglia, D. Su, W. Tong, *Adv. Energy Mater.* **2019**, *9*, 1902258; b) J. S. Kim, B. H. Kim, D. C. Kim, H. J. Lee, M. G. Kim, A. Maignan, B. Raveau, Y. W. Park, *J. Supercond.* **2004**, *17*, 183–186.
[30] H. Liu, Y. Chen, S. Hy, K. An, S. Venkatachalam, D. Qian, M. Zhang, Y. S. Meng, *Adv. Energy Mater.* **2016**, *6*, 1502143.

Manuscript received: September 19, 2022
Accepted manuscript online: December 1, 2022
Version of record online: December 22, 2022